

# Electronic structures and multi-orbital models of $\text{La}_3\text{Ni}_2\text{O}_7$ thin films at ambient pressure

Xunwu Hu<sup>1,2†</sup>, Wenyuan Qiu<sup>2†</sup>, Cui-Qun Chen<sup>2</sup>, Zhihui Luo<sup>2</sup>,  
Dao-Xin Yao<sup>2\*</sup>

<sup>1</sup>Department of Physics, College of Physics and Optoelectronic Engineering, Jinan University, Guangzhou, 510632, China.

<sup>2</sup>Center for Neutron Science and Technology, Guangdong Provincial Key Laboratory of Magnetoelectric Physics and Devices, State Key Laboratory of Optoelectronic Materials and Technologies, School of Physics, Sun Yat-Sen University, Guangzhou, 510275, China.

\*Corresponding author(s). E-mail(s): [yaodaوخ@mail.sysu.edu.cn](mailto:yaodaوخ@mail.sysu.edu.cn);

<sup>†</sup>These authors contributed equally to this work.

## Abstract

The recent discovery of superconductivity with a transition temperature  $T_c$  exceeding 40 K in  $\text{La}_3\text{Ni}_2\text{O}_7$  and  $(\text{La},\text{Pr})_3\text{Ni}_2\text{O}_7$  thin films at ambient pressure marks a significant breakthrough in the field of nickelate superconductors. Using density functional theory (DFT), we propose a double-stacked two-orbital effective model for  $\text{La}_3\text{Ni}_2\text{O}_7$  thin film based on the  $\text{Ni}-e_g$  orbitals. Our analysis of the Fermi surface reveals three electron pockets ( $\alpha, \alpha', \beta$ ) and two hole pockets ( $\gamma, \gamma'$ ), where the additional  $\alpha'$  and  $\gamma'$  pockets arise from inter-stack interactions. Furthermore, we introduce a high-energy model that incorporates  $\text{O}-p$  orbitals to facilitate future studies. Calculations of spin susceptibility within the random phase approximation (RPA) indicate that magnetic correlations are enhanced by nesting of the  $\gamma$  pocket, which is predominantly derived from the  $\text{Ni}-d_{z^2}$  orbital. Our results provide a theoretical foundation for understanding the electronic and magnetic properties of  $\text{La}_3\text{Ni}_2\text{O}_7$  thin films.

**Keywords:** Superconductivity, Nickelate, Thin film, Density function theory, Tight-binding model

# 1 Introduction

The discovery of superconductivity in the Ruddlesden-Popper (RP) bilayer nickelate  $\text{La}_3\text{Ni}_2\text{O}_7$  at a transition temperature  $T_c$  near 80 K under high pressure ( $\sim 14$  GPa) has generated significant interest in the field of unconventional superconductivity [1]. The subsequent observation of superconductivity in the trilayer nickelate  $\text{La}_4\text{Ni}_3\text{O}_{10}$  under similar conditions further underscores the universality of superconductivity in nickelates [2]. These discoveries have motivated extensive theoretical [3–38] and experimental [39–46] investigations into the microscopic mechanisms of unconventional superconductivity. However, the requirement of high pressure for superconductivity in  $\text{La}_3\text{Ni}_2\text{O}_7$  and  $\text{La}_4\text{Ni}_3\text{O}_{10}$  presents significant experimental challenges, which limit in-depth investigations. This has driven efforts to stabilize superconductivity under ambient pressure, facilitating a more comprehensive understanding of its underlying mechanisms.

Recent studies have reported superconductivity with  $T_c$  exceeding 40 K in  $\text{La}_3\text{Ni}_2\text{O}_7$  [47],  $(\text{La},\text{Pr})_3\text{Ni}_2\text{O}_7$  [48] thin films at ambient pressure, marking a significant breakthrough in nickelate superconductors. X-ray absorption spectroscopy (XAS) reveals that the Ni ions in  $\text{La}_3\text{Ni}_2\text{O}_7$  thin film retain a mixed valence state similar to the bulk form [47]. Furthermore, scanning transmission electron microscopy (STEM) confirms that their microscopic structure closely resembles that of the bulk phase of high pressure, characterized by an angle of apical Ni-O-Ni bonds approaching  $180^\circ$  [47]. In particular, the  $T_c$  in the thin film is tunable via the in-plane lattice constant but remains relatively insensitive to the out-of-plane parameter. DFT calculations [48–51] and angle-resolved photoemission spectroscopy (ARPES) measurements [52] suggest that Ni- $d_{x^2-y^2}$  and Ni- $d_{z^2}$  orbitals contribute states near the Fermi level, highlighting the similarity between thin film and bulk system in terms of electronic structure and superconducting properties. Despite these advances, most theoretical studies have relied on simplified half-unit-cell (Half-UC) slab model [53, 54], which may not fully capture the effects of dimensionality on the electronic structure. A more comprehensive approach incorporating full-unit-cell slab model is therefore needed to provide a more accurate description of this system.

In this paper, we employ slab models of  $\text{La}_3\text{Ni}_2\text{O}_7$  thin films to investigate their electronic structures across various thicknesses, including three-unit-cell (Three-UC), one-unit-cell (One-UC), and Half-UC configurations. Except for the Half-UC case, each slab model retains a complete unit cell (UC), with the two bilayers denoted as Stack 1 and Stack 2, enabling a systematic exploration of the relationship between dimensionality and electronic properties. Using first-principles calculations, we propose a double-stacked two-orbital effective model for the One-UC slab structure, based on Ni- $e_g$  orbitals. Our analysis reveals the presence of three electron pockets ( $\alpha, \alpha', \beta$ ) and two hole pockets ( $\gamma, \gamma'$ ) on the Fermi surface, where inter-stack interactions give rise to the additional  $\alpha'$  and  $\gamma'$  pockets. Furthermore, we extend our model by incorporating O- $p$  orbitals into a high-energy framework to facilitate future studies. Spin susceptibility calculations within the RPA indicate pronounced magnetic correlations, primarily driven by nesting effects of the  $\gamma$  pocket, which is predominantly derived from the Ni- $d_{z^2}$  orbital. Our results provide theoretical framework for understanding the

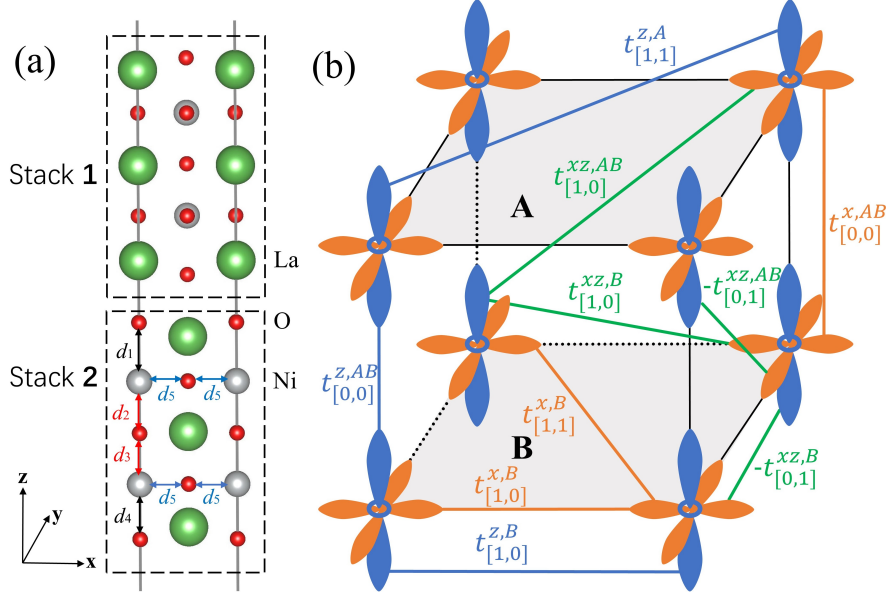


**Fig. 1** (a) The One-UC slab structure of  $\text{La}_3\text{Ni}_2\text{O}_7$  thin film, where the two bilayers are labeled as Stack 1 and Stack 2. Green, gray, and red spheres represent La, Ni, and O atoms, respectively. The outer-apical ( $d_1$  and  $d_4$ ), inner-apical ( $d_2$  and  $d_3$ ), and in-plane ( $d_5$ ) Ni-O bond distances are indicated by black, red, and blue arrows, respectively. (b) Schematic illustration of the hopping parameters in the  $\text{La}_3\text{Ni}_2\text{O}_7$  thin film, highlighting the  $\text{Ni}-d_{x^2-y^2}$  (orange) and  $d_{z^2}$  (blue) orbitals. Only the nearest-neighbor hopping parameters are shown.

interplay among the dimensionality, magnetism, and superconductivity in  $\text{La}_3\text{Ni}_2\text{O}_7$  thin films, offering key insights for future theoretical and experimental investigations.

## 2 Results

### 2.1 Slab structures

We begin our investigation of the  $\text{La}_3\text{Ni}_2\text{O}_7$  thin films by modeling the slab structures using DFT calculations. Bulk  $\text{La}_3\text{Ni}_2\text{O}_7$  belongs to the  $n = 2$  Ruddlesden-Popper phase, characterized by a UC comprising two corner-sharing  $\text{NiO}_6$  octahedra bilayers stacking along the  $c$  axis [1]. In its thin-film form,  $\text{La}_3\text{Ni}_2\text{O}_7$  adopts a tetragonal structure similar to the high-pressure bulk phase, distinguished by an apical Ni-O-Ni bond angle approaching  $180^\circ$  [47]. To systematically explore the structural and electronic properties of  $\text{La}_3\text{Ni}_2\text{O}_7$  thin films, we consider slab structures of varying thicknesses along the out-of-plane direction, including Three-UC, One-UC, and Half-UC slabs. To minimize interactions between preiodic images, a vacuum spacing exceeding  $16 \text{ \AA}$  is introduced along the  $c$  axis.

The One-UC slab consists of two stacked  $\text{NiO}_6$  octahedra bilayers, which can adopt two distinct stacking configurations, Stack 1 and Stack 2, as illustrated in Fig. 1(a). In all slab structures, we fix the in-plane lattice constant of  $a = 3.77 \text{ \AA}$  [47]. The Ni-O bond lengths, labeled as  $d_1$ ,  $d_2$ ,  $d_3$ ,  $d_4$ , and  $d_5$  in Fig. 1(a), are summarized in

**Table 1** The Ni-O bond lengths ( $d$ ) in  $\text{NiO}_6$  octahedra of  $\text{La}_3\text{Ni}_2\text{O}_7$  slab structures under  $U = 0$  eV and  $U = 2$  eV. The unit of  $d$  are in  $\text{\AA}$ .

$U$ (eV)	Stack	$d$	Three-UC	One-UC	Half-UC
$U = 0$	1	$d_1$	2.292	2.120	2.116
		$d_2$	1.965	1.973	2.003
		$d_3$	1.965	2.003	2.003
		$d_4$	2.282	2.276	2.116
		$d_5$	1.885	1.885	1.885
	2	$d_1$	2.282	2.276	–
		$d_2$	1.965	2.003	–
		$d_3$	1.965	1.973	–
		$d_4$	2.292	2.120	–
		$d_5$	1.885	1.885	–
$U = 2$	1	$d_1$	2.308	2.133	2.120
		$d_2$	1.960	1.944	1.996
		$d_3$	1.960	2.012	1.996
		$d_4$	2.307	2.364	2.120
		$d_5$	1.885	1.885	1.885
	2	$d_1$	2.307	2.364	–
		$d_2$	1.960	2.012	–
		$d_3$	1.960	1.944	–
		$d_4$	2.308	2.133	–
		$d_5$	1.885	1.885	–

Table 1 for different slab structures and electronic correlation strength ( $U = 0$  eV and  $U = 2$  eV). For clarity, only the bond distances of the middle UC are reported for the Three-UC slab structure.

For  $U = 0$  eV, the in-plane Ni-O bond ( $d_5$ ) is the shortest, while the outer-apical Ni-O bonds ( $d_1$  and  $d_4$ ) are the longest, consistent with the high-pressure phase of  $\text{La}_3\text{Ni}_2\text{O}_7$ . Different slab structures yield nearly identical results in terms of bond lengths. In the Three-UC and One-UC slabs,  $d_1$  and  $d_4$  vary across stacking configurations, while  $d_2$  and  $d_3$  also exhibit stack-dependent variations, indicating symmetry breaking between different stacks. The Ni-O bond lengths in these slabs follow a specific symmetry relation: in Stack 1,  $d_1, d_2, d_3, d_4$  correspond to  $d_4, d_3, d_2, d_1$  in Stack 2. In contrast, the Half-UC slab exhibits a distinct structural behavior, characterized by Ni-O bond lengths that are symmetric about the central oxygen atom, differing from the asymmetric distortions observed in the other slab structures. This difference arises from the underlying structural symmetry. In Half-UC, the slab possesses  $m_z$  symmetry, with the mirror plane located between the two NiO layers. This symmetry enforces bond length equivalence with respect to the mirror plane, resulting in two nonequivalent vertical bond lengths. However, the One-UC and Three-UC slabs exhibit a different symmetry operation,  $\{m_z | \frac{1}{2}, \frac{1}{2}, \frac{1}{2}\}$ , where the mirror plane lies between two stacks. This symmetry allows for bond length variations within each individual stack, leading to distinct vertical bond lengths across the three stacks in the Three-UC slab, whereas only one stack exhibits such variations in the One-UC slab. This symmetry



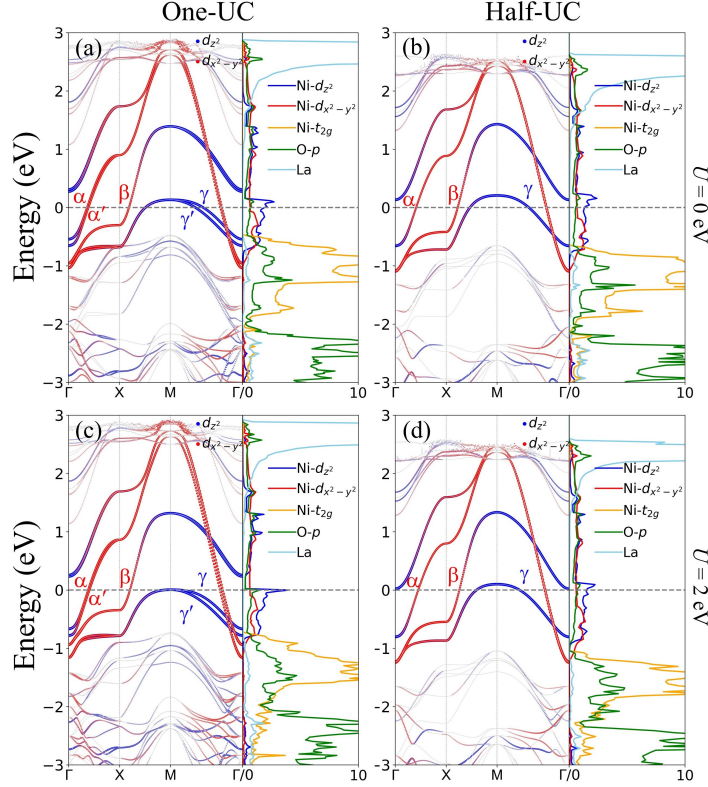


**Fig. 2** The DFT-calculated band structures and partial density of states (PDOS) of  $\text{La}_3\text{Ni}_2\text{O}_7$  thin films, where panels (a)–(c) correspond to  $U = 0$  eV and panels (d)–(f) correspond to  $U = 2.5$  eV. The contributions from the  $\text{Ni}-d_{x^2-y^2}$  and  $d_{z^2}$  orbitals are highlighted in blue and red, respectively, while  $\text{Ni}-t_{2g}$ ,  $\text{O}-p$ , and  $\text{La}$  states are represented in orange, green, and cyan, respectively. The Fermi level ( $E_F$ ) is set to 0 eV.

distinction is further reflected in the hopping parameters, influencing the electronic properties of the system.

For  $U = 2$  eV, electron correlation significantly influences the outer-apical Ni-O bond lengths ( $d_1$  and  $d_4$ ) in the Three-UC and One-UC slabs, whereas its effect is negligible in the Half-UC slab. Meanwhile, the in-plane Ni-O bond length ( $d_5$ ) remains relatively stable in all configurations. These structural modifications are expected to have a pronounced impact on the electronic structures, which will be examined in detail in the following subsection. These findings highlight the critical role of interlayer interactions in determining the structural properties, which cannot be adequately captured by the Half-UC slab.

## 2.2 Electronic structures

We now investigate the electronic structures of  $\text{La}_3\text{Ni}_2\text{O}_7$  thin films based on DFT calculations. For  $U = 0$  eV, the band structure and projected density of states (PDOS) of the One-UC slab exhibit a clear metallic character, as shown in Fig. 2(a). The

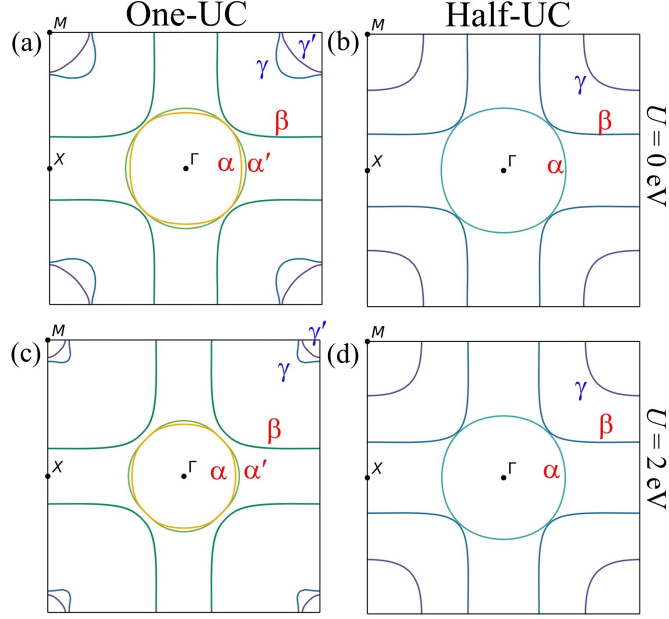


**Fig. 3** The DFT-calculated two-dimensional Fermi surfaces of  $\text{La}_3\text{Ni}_2\text{O}_7$  thin films for different slab models: (a)(c) One-UC, and (b)(d) Half-UC. The upper panels show results at Hubbard  $U = 0$  eV, while the lower panels correspond to calculations at  $U = 2.0$  eV.

electronic states near the Fermi level ( $E_F$ ) are primarily composed of  $\text{Ni}-d_{x^2-y^2}$  and  $\text{Ni}-d_{z^2}$  orbitals, which are well separated from the lower-energy  $\text{Ni}-t_{2g}$  orbitals. Moreover, these  $\text{Ni}-d$  orbitals exhibit hybridization with  $\text{O}-p$  orbitals within the energy range of  $-2$  eV to  $2$  eV. Due to interlayer hybridization, the  $\text{Ni}-d_{z^2}$  electronic states form bonding and antibonding bands, located below and above  $E_F$ , respectively. Additionally, the La-derived states make minimal contributions to the electronic states at  $E_F$ . The electronic structures of the Three-UC slab exhibit a similar behavior to that of the One-UC slab, as shown in Fig. A1(a) in Appendix A. Notably, the reduced structural symmetry in thin films induces a splitting of  $\text{Ni}-d_{z^2}$  bonding bands along the  $M - \Gamma$  direction, leading to the formation of distinct electronic pockets near the  $M$  point [See Fig. 3(a)]. In contrast, the Half-UC slab, which retains higher structural symmetry, does not exhibit such splitting in the  $\text{Ni}-d_{z^2}$  bonding bands [see Fig. 2(b)].

For  $U = 2$  eV, the  $\text{Ni}-d_{z^2}$  bonding bands shift downward and approach  $E_F$ . Consequently, the density of states of  $\text{Ni}-d_{z^2}$  attains a maximum at  $E_F$  in the One-UC slab, as shown in Fig. 2(c). A similar downward shift is observed in the electronic structure of the Three-UC slab, where the  $\text{Ni}-d_{z^2}$  bonding bands move closer to  $E_F$ , as demonstrated in Fig. A1(b). This behavior corresponds to the metallization of the lower  $\sigma$  bonds in the high-pressure phase of bulk  $\text{La}_3\text{Ni}_2\text{O}_7$ . These results indicate that the electronic structure of  $\text{La}_3\text{Ni}_2\text{O}_7$  thin films closely resembles that of the high-pressure phase of the bulk material, which may provide insight into the emergence of high-temperature superconductivity in thin films. In contrast, the  $E_F$  in the Half-UC

slab exhibits only a slight downward shift, as illustrated in Fig. 2(d). Previous studies on bulk  $\text{La}_3\text{Ni}_2\text{O}_7$  have reported that DFT calculations with  $U = 3.5$  eV yield results that are in good agreement with experimental observations [39]. To further explore this, we also consider the case of  $U = 3.5$  eV. Under this condition, the  $\text{Ni}-d_{z^2}$  bonding bands in the Three-UC and One-UC slabs shift further downward, moving below  $E_F$ , as shown in Figs. A1(c) and A2(a). However, in the Half-UC slab,  $E_F$  still crosses the  $\text{Ni}-d_{z^2}$  bonding bands, as shown in Fig. A2(b).

Figure 3 presents the evolution of the Fermi surface in  $\text{La}_3\text{Ni}_2\text{O}_7$  thin films under different slab configurations and Hubbard  $U$ . Panels (a) and (c) correspond to  $U = 0$  eV, while panels (b) and (d) correspond to  $U = 2$  eV. For  $U = 0$  eV, the Fermi surface of the One-UC slab consists of three electron pockets ( $\alpha, \alpha', \beta$ ) and two hole pockets ( $\gamma, \gamma'$ ), as shown in Fig. 3(a). Notably, the  $\gamma$  and  $\gamma'$  pockets are primarily derived from the  $\text{Ni}-d_{z^2}$  orbital. The splitting of the  $\text{Ni}-d_{z^2}$  and  $\text{Ni}-d_{x^2-y^2}$  states along the  $M - \Gamma$  and  $X - \Gamma$  directions gives rise to the additional  $\alpha'$  and  $\gamma'$  pockets. This splitting originates from inter-stack interactions induced by the reduced structural symmetry in thin films. In contrast, there are two electron pockets ( $\alpha, \beta$ ) and one hole pocket ( $\gamma$ ) on the Fermi surface in the Half-UC slab, as shown in Fig. 3(b).

For  $U = 2$  eV, as the  $\text{Ni}-d_{z^2}$  bonding bands in the One-UC slab shift downward and approach  $E_F$ , there is a significant reduction in the spatial extent of the hole pockets  $\gamma$  and  $\gamma'$  around the  $M$  point in the Brillouin zone, as shown in Fig. 3(c). In contrast, the Fermi surface geometry in the Half-UC slab exhibits minimal changes, as depicted in Fig. 3(d).

### 2.3 Two-orbital models

Based on the previous subsections, the thickness of the slab model significantly influences the Ni-O bond lengths, which in turn affect the electronic structure. Experimental samples typically have a thickness of One-UC–Three-UC, and calculations for the Three-UC slab are expected to more closely reflect the experimental conditions. However, due to the complexity of the Three-UC slab model, we have chosen to construct the tight-binding (TB) model using the One-UC slab, which captures the main features of the electronic band structure observed in the Three-UC slab. The Half-UC slab is also considered for comparison.

Building on the electronic structures obtained from our DFT calculations, we first focus on the double-stacked two-orbital model for the One-UC slab. This model incorporates the  $\text{Ni}-d_{x^2-y^2}$  and  $\text{Ni}-d_{z^2}$  orbitals within the framework of the maximally localized Wannier functions Hamiltonian. The total Hamiltonian is given by

$$\begin{aligned}\mathcal{H} &= \mathcal{H}_0 + \mathcal{H}_U, \\ \mathcal{H}_0 &= \sum_{\mathbf{k}\sigma} \Psi_{\mathbf{k}\sigma}^\dagger H(\mathbf{k}) \Psi_{\mathbf{k}\sigma}.\end{aligned}\tag{1}$$

Here  $\mathcal{H}_0$  denotes the TB Hamiltonian derived from the Wannier downfolding procedure, while  $\mathcal{H}_U$  represents the Coulomb interaction term [55].

The basis of the model is defined as  $\Psi_\sigma = (d_{1Ax\sigma}, d_{1Az\sigma}, d_{1Bx\sigma}, d_{1Bz\sigma}, d_{2Ax\sigma}, d_{2Az\sigma}, d_{2Bx\sigma}, d_{2Bz\sigma})^T$ , where the field operator

**Table 2** Hopping parameters for the One-UC slab model of  $\text{La}_3\text{Ni}_2\text{O}_7$  thin film.  $t_{A/B,[00]}^x$  and  $t_{A/B,[00]}^z$  represent the site energies for the  $d_{x^2-y^2}$  and  $d_{z^2}$  orbitals in layer A and B, respectively. The numbers in the brackets correspond to parameters of the high-pressure phase of bulk  $\text{La}_3\text{Ni}_2\text{O}_7$  [3]. The units are eV.

Index	Layer	$i$	$j$	$t_{[ij]}^x$	$t_{[ij]}^z$	$t_{[ij]}^{xz}$
Stack 1	A	0	0	0.844(0.776)	0.519(0.409)	0.000
		1	0	-0.462(-0.483)	-0.134(-0.110)	0.228(0.239)
		1	1	0.075(0.069)	-0.021(-0.017)	0.000
		2	0	-0.053	-0.008	0.017
		3	0	-0.013	-0.003	0.000
	B	0	0	0.918	0.344	0.000
		1	0	-0.460	-0.083	0.201
		1	1	0.075	-0.015	0.000
		2	0	-0.055	-0.013	0.023
		3	0	-0.012	-0.002	0.000
	AB	0	0	0.005(0.005)	-0.550(-0.635)	0.000
		1	0	-0.000	0.020	-0.031(-0.034)
Stack 2	A	0	0	0.918	0.344	0.000
		1	0	-0.460	-0.083	0.201
		1	1	0.075	-0.015	0.000
		2	0	-0.055	-0.013	0.023
		3	0	-0.012	-0.002	0.000
	B	0	0	0.844	0.519	0.000
		1	0	-0.462	-0.134	0.228
		1	1	0.075	-0.021	0.000
		2	0	-0.053	-0.008	0.017
		3	0	-0.013	-0.003	0.000
	AB	0	0	0.005	-0.550	0.000
		1	0	0.000	0.020	-0.029

$d_{s\sigma}$  annihilates an electron in the state  $s$  with spin  $\sigma$ . The indices are assigned as follows: 1/2 label the stacked layers,  $A/B$  correspond to the bilayer sublattices, and  $x/z$  denote the  $d_{x^2-y^2}$  and  $d_{z^2}$  orbitals, respectively. The labeling convention is illustrated in Fig. 1(b).

The TB Hamiltonian  $H(\mathbf{k})$  takes the form

$$\begin{aligned}
H(\mathbf{k}) &= \begin{pmatrix} H^1(\mathbf{k}) & H^{12}(\mathbf{k}) \\ H^{12}(\mathbf{k}) & H^2(\mathbf{k}) \end{pmatrix}, \\
H^{1/2}(\mathbf{k}) &= \begin{pmatrix} H_A^{1/2}(\mathbf{k}) & H_{AB}^{1/2}(\mathbf{k}) \\ H_{AB}^{1/2}(\mathbf{k}) & H_B^{1/2}(\mathbf{k}) \end{pmatrix}, \\
H_{A/B}^{1/2}(\mathbf{k}) &= \begin{pmatrix} H_{A/B}^{1/2,x}(\mathbf{k}) & H_{A/B}^{1/2,xz}(\mathbf{k}) \\ H_{A/B}^{1/2,xz}(\mathbf{k}) & H_{A/B}^{1/2,z}(\mathbf{k}) \end{pmatrix},
\end{aligned}$$

**Table 3** Hopping parameters for Half-UC slab model of  $\text{La}_3\text{Ni}_2\text{O}_7$  thin film.  $t_{A,[00]}^x$ ,  $t_{A,[00]}^z$  are the site energies for  $d_{x^2-y^2}$  and  $d_{z^2}$  orbitals in layer A. The units are eV.

Index	Layer	$i$	$j$	$t_{[ij]}^x$	$t_{[ij]}^z$	$t_{[ij]}^{xz}$
Stack 1	A	0	0	0.756	0.389	0.000
		1	0	-0.445	-0.131	0.221
		1	1	0.060	-0.015	0.000
		2	0	-0.057	-0.011	0.019
		3	0	-0.009	-0.004	0.000
	AB	0	0	0.000	-0.503	0.000
		1	0	0.000	0.026	-0.031

$$H_{AB}^{1/2}(\mathbf{k}) = \begin{pmatrix} H_{AB}^{1/2,x}(\mathbf{k}) & H_{AB}^{1/2,xz}(\mathbf{k}) \\ H_{AB}^{1/2,xz}(\mathbf{k}) & H_{AB}^{1/2,z}(\mathbf{k}) \end{pmatrix}. \quad (2)$$

The matrix elements are defined as follows:

$$\begin{aligned}
H_{A/B}^{1/2,x/z}(\mathbf{k}) &= 2t_{A/B,[1,0]}^{1/2,x/z} (\cos k_x + \cos k_y) \\
&\quad + 2t_{A/B,[2,0]}^{1/2,x/z} (\cos 2k_x + \cos 2k_y) \\
&\quad + 2t_{A/B,[3,0]}^{1/2,x/z} (\cos 3k_x + \cos 3k_y) \\
&\quad + 4t_{A/B,[1,1]}^{1/2,x/z} \cos k_x \cos k_y + \epsilon_{A/B}^{1/2,x/z}, \\
H_{A/B}^{1/2,xz}(\mathbf{k}) &= 2t_{A/B,[1,0]}^{1/2,xz} (\cos k_x - \cos k_y) \\
&\quad + 2t_{A/B,[2,0]}^{1/2,xz} (\cos 2k_x - \cos 2k_y), \\
H_{AB}^{1/2,x/z}(\mathbf{k}) &= t_{AB,[0,0]}^{1/2,x/z} + 2t_{AB,[1,0]}^{1/2,x/z} (\cos k_x - \cos k_y), \\
H_{AB}^{1/2,xz}(\mathbf{k}) &= 2t_{AB,[1,0]}^{1/2,xz} (\cos k_x - \cos k_y), \\
H_{AB}^{12,z}(\mathbf{k}) &= 4t_{AB}^{12,z} [\cos(k_x/2) \cos(k_y/2)].
\end{aligned}$$

Here  $H_{A/B}^{1/2,x/z}(\mathbf{k})$  and  $H_{AB}^{1/2,x/z}(\mathbf{k})$  describe intralayer and interlayer hopping within the same orbitals ( $d_{x^2-y^2}$  or  $d_{z^2}$ ), respectively, while  $H_{A/B}^{1/2,xz}(\mathbf{k})$  and  $H_{AB}^{1/2,xz}(\mathbf{k})$  represent intralayer and interlayer hybridization between  $d_{x^2-y^2}$  and  $d_{z^2}$  orbitals. Additionally,  $H_{AB}^{12,z}(\mathbf{k}) = 4t_{AB}^{12,z} \cos(k_x/2) \cos(k_y/2)$  describes inter-stack hopping within the  $d_{z^2}$  orbital, with a corresponding hopping parameter  $t_{AB}^{12,z} = -0.025$ . Hopping parameters for the One-UC slab model of  $\text{La}_3\text{Ni}_2\text{O}_7$  thin film are summarized in Table 2.

For the single-stacked two-orbital model of the Half-UC slab, the system exhibits layer symmetry and the absence of inter-stack coupling, as characterized by the conditions  $H^1(\mathbf{k}) = H^2(\mathbf{k})$ ,  $H^{12}(\mathbf{k}) = 0$ , and  $H_A^1(\mathbf{k}) = H_B^1(\mathbf{k})$ . These conditions indicate

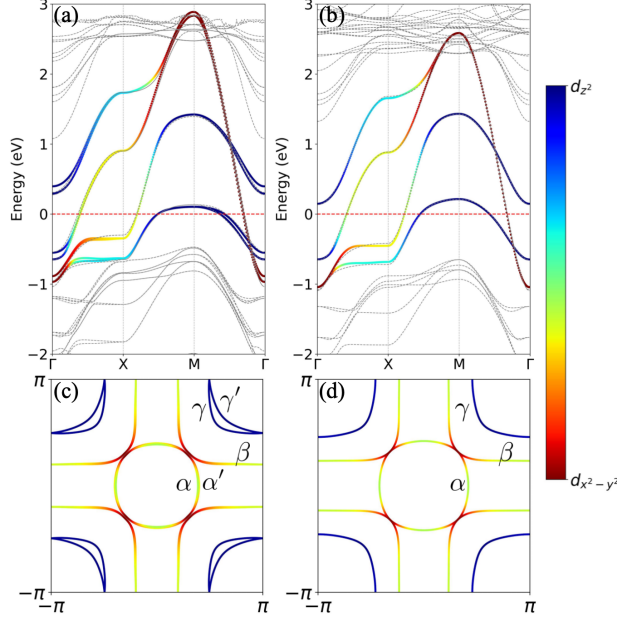


**Fig. 4** Band structure and Fermi surface of the two-orbital models for  $\text{La}_3\text{Ni}_2\text{O}_7$  thin films. Panels (a) and (c) correspond to the double-stacked two-orbital model for the One-UC slab, while panels (b) and (d) correspond to the single-stacked two-orbital model for the Half-UC slab. The orbital contributions of  $d_{x^2-y^2}$  and  $d_{z^2}$  are highlighted in red and blue, respectively. In (a) and (b), the gray lines represent the DFT-calculated band structures at  $U = 0$  eV. The  $E_F$  is set to 0 eV.

that the Hamiltonians of the individual layers are identical, there is no direct coupling between the stacks, and the interfacial hopping parameters are equivalent for both sublattices. The corresponding hopping parameters for the Half-UC slab model of  $\text{La}_3\text{Ni}_2\text{O}_7$  thin film are provided in Table 3.

Using the TB parameters listed in Tables 2 and 3, we present the resulting band structure and Fermi surface for both One-UC and Half-UC slabs. As shown in Fig. 4(a), the model for the One-UC slab accurately reproduces the DFT band structure near the  $E_F$ . Notably, we observe a splitting of the  $\text{Ni}-d_{z^2}$  bonding bands along the  $M - \Gamma$  direction, which originates from inter-stack interaction, specifically  $t_{AB}^{12,z}$ . Regarding the Fermi surface, we identify three electron pockets  $\alpha, \alpha', \beta$  and two hole pockets  $\gamma, \gamma'$ , as illustrated in Fig. 4(c). The  $\alpha, \alpha', \beta$ -pocket exhibit mixed orbital character, while the  $\gamma, \gamma'$ -pockets are primarily dominated by the  $d_{z^2}$  orbital state. Our results indicate that the electronic structure of  $\text{La}_3\text{Ni}_2\text{O}_7$  thin film at ambient pressure closely resembles that of the high-pressure bulk phase. A key structural aspect is the in-plane lattice constant of the thin film, which is  $3.77\text{\AA}$ —large than the pseudo-tetragonal bulk value of  $3.715\text{\AA}$ . This lattice expansion may account for the lower  $T_c$  of the thin film compared to the bulk, suggesting that strain engineering could be a viable approach to enhancing  $T_c$  by further compressing the in-plane lattice constant. Furthermore, we note that the interlayer hopping amplitude  $t_{AB,[00]}^z = -0.550$  is 1.19 times larger than the intralayer nearest-neighbor hopping  $t_1^x = -0.462$ . However, it remains 13.4%

**Table 4** TB parameters for Wannier downfolding of the twenty-two-orbital model. Only the parameters of Stack 1 are presented, due to the symmetry between Stack 1 and Stack 2. See the schematic in Fig. A4 for further details.

Stack 1			
Hopping	$Ad_{z^2} - p_{z'}$	$Ad_{z^2} - p_z$	$Ad_{z^2} - Ap_{x/y}$
	1.304	-1.478	0.692
Hopping	$Bd_{z^2} - p_{z''}$	$Bd_{z^2} - p_z$	$Bd_{z^2} - Bp_{x/y}$
	-1.105	1.435	0.629
Hopping	$Ap_x - Ap_y$	$Ap_{x/y} - p_z$	$Ap_{x/y} - p_{z'}$
	-0.560	-0.435	0.443
Hopping	$Bp_x - Bp_y$	$Bp_{x/y} - p_z$	$Bp_{x/y} - p_{z''}$
	-0.575	0.428	-0.380
Hopping	$Ad_{x^2-y^2} - Ap_{x/y}$	$Bd_{x^2-y^2} - Bp_{x/y}$	
	$\pm 1.480$	$\pm 1.479$	
Site	$Ad_{z^2}/Bd_{z^2}$	$Ad_{x^2-y^2}/Bd_{x^2-y^2}$	$p_z$
Energy	-1.104/-1.036	-1.001/-0.9223	-4.078
Site	$Ap_{x/y}/Bp_{x/y}$	$Ap_{z'}/Bp_{z''}$	
Energy	-4.669/-4.630	-2.730/-3.224	

smaller than its bulk counterpart ( $t_{AB,[00]}^z = -0.635$ ). This reduction in interlayer coupling suggests a possible weakening of unconventional pairing in the thin film compared to the bulk.

For the Half-UC slab model, no splitting in the Ni- $d_{z^2}$  bonding bands [see Fig. 4(b)]. Consequently, the Fermi surface consists of two electron pockets  $\alpha, \beta$  and one hole pocket  $\gamma$ , as illustrated in Fig. 4(d). Additionally, the interlayer hopping amplitude  $t_{AB,[00]}^z = -0.503$  is 1.13 times larger than the intralayer nearest-neighbor hopping  $t_1^x = -0.445$ , yet it remains 21% smaller than its bulk counterpart. Notably, when we set  $t_{AB}^{12,z} = 0$ , no splitting is observed in the band structure or the Fermi surface of the One-UC slab, as shown in Fig. A3.

## 2.4 High-energy $dp$ models

To explicitly incorporate the physics of O- $p$  orbitals, we introduce high-energy  $dp$  models: a double-stacked eleven-orbital model for the One-UC slab (referred to as twenty-two-orbital model) and a single-stacked eleven-orbital model for the Half-UC slab (referred to as the eleven-orbital model). In both models, the basis for

**Table 5** TB parameters for the Wannier downfolding of the eleven-orbital model. Only the parameters of Layer A are presented, due to the symmetry between Layers A and B. See the schematic in Fig. A4 for further details.

Stack 1				
Hopping	$Ad_{z^2} - p_z$	$Ad_{z^2} - p_{z'}$	$Ad_{z^2} - Ap_{x/y}$	$Ad_{x^2-y^2} - Ap_{x/y}$
	-1.423	1.296	0.697	$\pm 1.482$
Hopping	$Ap_x - Ap_y$	$Ap_{x/y} - p_z$	$Ap_{x/y} - p_{z'}$	
	-0.589	0.483	-0.440	
Site	$Ad_{z^2}$	$Ad_{x^2-y^2}$	$Ap_{x/y}$	$p_z$
energy	-1.198	-1.127	-4.790	-4.150
Site	$Ap_{z'}/z''$			
energy	-2.927			

Stack 1 is given by  $\Psi = (d_{Az}, d_{Bz}, d_{Ax}, d_{Bx}, d_{Ap_x}, d_{Bp_x}, d_{Ap_y}, d_{Bp_y}, d_{p_z}, d_{p_{z'}}, d_{p_{z''}})^T$ , which includes four in-plane orbitals ( $p_{Ax}, p_{Ay}, p_{Bx}, p_{By}$ ) and three apical orbitals ( $p_z, p_{z'}, p_{z''}$ ), as illustrated in Fig. A4. Here,  $A$  and  $B$  denote the bilayer sublattices.

The TB parameters of the twenty-two-orbital model are listed in Table 4, while those of the eleven-orbital model are provided in Table 5. Due to the symmetry between Stack 1 and Stack 2, only the parameters for Stack 1 are presented, and inter-stack hopping terms are not considered. Both models incorporate hopping interactions arising from  $pd, pp$  orbital overlaps. Based on the TB parameters, we present the resulting band structure and Fermi surface for both the One-UC and Half-UC slabs, as shown in Fig. 5. The resulting band structure in Fig. 5 covers an energy range akin to that of Fig. 4 and can also reproduce the main features at  $E_F$ . Moreover, we find a strong hopping of 1.296 for eleven-orbital model and of 1.304/1.105 for twenty-two-orbital model between  $d_{z^2}$  and two apical  $p_{z'}, p_{z''}$  that lie outside the bilayer, which manifest as two hole baths for NiO<sub>2</sub> plane and could be further integrated out in a Löwdin downfolding technique [56]. The high-energy models will be useful for further study of electronic correlations in the dynamic mean field theory framework and other methods.

## 2.5 Spin susceptibility for two-orbital models

With the multi-orbital Hubbard model defined above, we investigate the magnetic response and Fermi surface nesting by calculating the spin susceptibility at the RPA level. Given that inter-stack hoppings are weak, we neglect them in our analysis. The resulting Fermi surface and energy bands in the absence of inter-stack hopping are provided in the Appendix A3.

To better demonstrate the Fermi surface nesting relations associated with the bilayer structure, we define the even and odd magnetic susceptibilities as:  $\chi^{e/o} =$



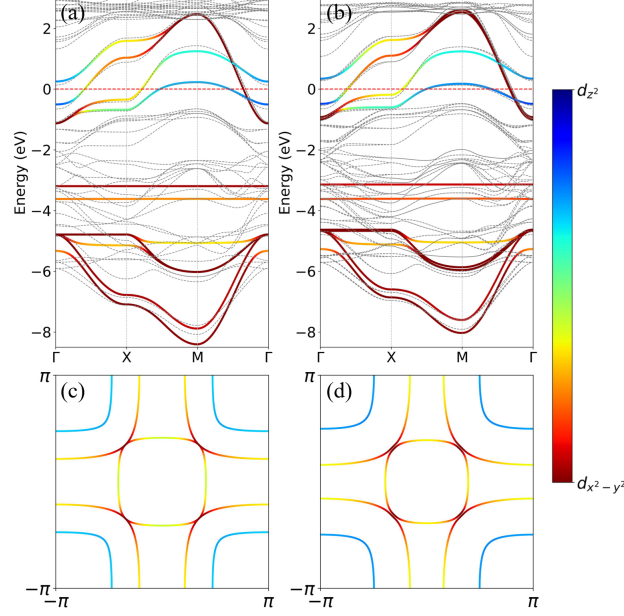
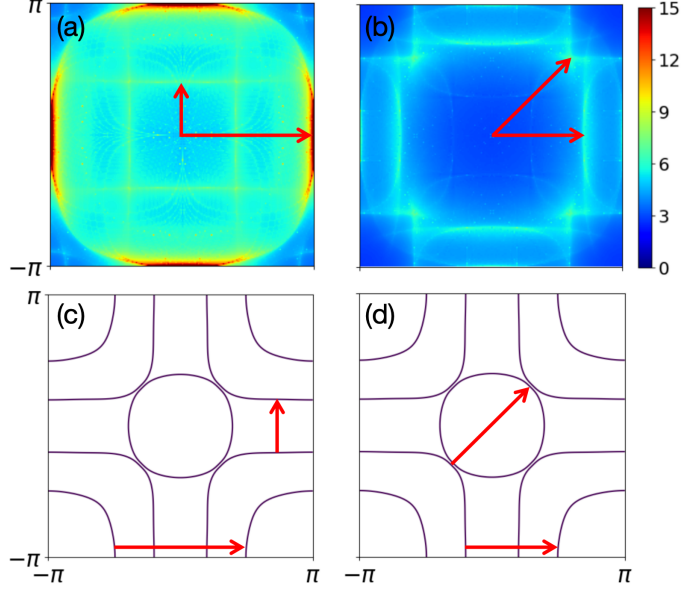


**Fig. 5** Band structure (a)(b) and Fermi surface (c)(d) of TB models including oxygen orbitals for  $\text{La}_3\text{Ni}_2\text{O}_7$  thin films. Panels (a) and (c) correspond to the eleven-orbital model for the Half-UC slab, while panels (b) and (d) correspond to the twenty-two-orbital model for the One-UC slab. The orbital weights of  $d_{x^2-y^2}$  and  $d_{z^2}$  are indicated in red and blue, respectively. The gray lines in (a) and (b) represent the DFT-calculated band structures at  $U = 0$  eV. The  $E_F$  is set to 0 eV.

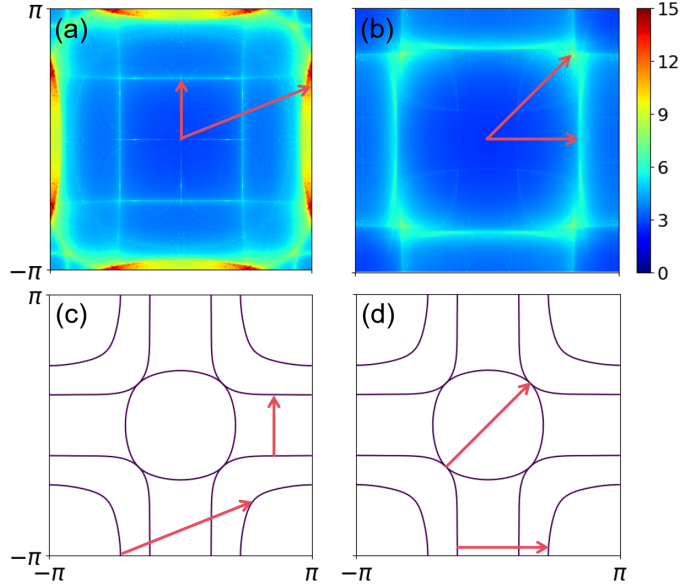
$\chi_{||} \pm \chi_{\perp}$ , with  $\chi_{||}$  and  $\chi_{\perp}$  representing intralayer and interlayer contributions, respectively. The definitions and computational details are available in the Methods section. Physically, it is easily proved that the  $\chi^e$  originates from nestings within the bonding ( $\alpha, \gamma$ ) and within the antibonding ( $\beta$ ) bands, while  $\chi^o$  originates solely from nestings between the bonding and antibonding bands [57].

Figure 6 presents the static RPA spin susceptibility  $\chi^{e/o}(\mathbf{q}, \omega = 0)$  for the double-stacked two-orbital model, computed with  $U = 0.7$  eV,  $J_H = 0.2$  eV, and temperature  $T = 0.1$  K. In the even channel, we observe a strong response near the  $X$  point, indicating nesting within the  $\gamma$  pocket, along with additional nesting within the  $\beta$  pocket. In the odd channel, nesting is evident between the  $\beta$  and  $\gamma$  pockets, as well as between the  $\alpha$  and  $\beta$  pockets.

Figure 7 presents the spin susceptibility for the single-stacked two-orbital model, calculated using  $U = 0.8$  eV,  $J_H = 0.2$  eV and  $T = 0.1$  K. The Fermi surface nesting patterns in the odd channel closely resemble those of the double-stacked model. In the even channel, nesting primarily occurs within the  $\gamma$  and  $\beta$  pockets, whereas in the odd channel, significant nesting is observed between the  $\gamma$  and  $\beta$  pockets, as well as between the  $\alpha$  and  $\beta$  pockets. The observed differences in  $\chi^{e/o}$  between the double-stacked and single-stacked models can be attributed to their distinct Fermi surface geometries.



**Fig. 6** (a) and (b) illustrate  $\chi^e$  and  $\chi^o$  of the double-stacked two-orbital model, respectively, computed with interaction parameters  $U = 0.7$  eV and  $J_H = 0.2$  eV at a temperature  $T = 0.1$  K. (c) and (d) depict the Fermi surface of the double-stacked two-orbital model, with red arrows indicating the nesting vectors.



**Fig. 7** (a) and (b) show  $\chi^e$  and  $\chi^o$  of the single-stacked two-orbital model, respectively, calculated with interaction parameters  $U = 0.8$  eV and  $J_H = 0.2$  eV at a temperature  $T = 0.1$  K. (c) and (d) present the Fermi surface of the single-stacked two-orbital model, with red arrows indicating the nesting vectors.

## 3 Methods

### 3.1 First-principles calculations

Our first-principles calculations are performed using the DFT as implemented in the Vienna *ab initio* simulation package (VASP) [58, 59]. The exchange-correlation interactions are treated within the generalized gradient approximation (GGA) using the Perdew-Burke-Ernzerhof (PBE) functional [60]. The projector augmented-wave (PAW) method [61] is employed with a plane-wave cutoff energy of 600 eV. Structural relaxation and electronic self-consistent calculations are conducted on a  $\Gamma$ -centered  $12 \times 12 \times 1$   $k$ -points mesh using the Monkhorst-Pack scheme, while a denser  $k$ -points grid of  $27 \times 27 \times 1$  is used for Fermi surface calculations. The atomic positions are fully relaxed until the residual forces on each atom are less than 0.005 eV/Å, and the electronic self-consistency convergence criterion is set to  $10^{-6}$  eV.

To construct effective models, maximally localized Wannier functions are obtained using the Wannier90 code [62–64]. For DFT +  $U$  calculations [65], an effective Hubbard  $U$  is applied to the Ni 3d orbitals.

### 3.2 Hamiltonian of high-energy $dp$ models

For the twenty-two-orbital model, we do not consider the hoppings between orbitals in different stacks. So the hamiltonian of twenty-two-orbital model take the same form as the one for the eleven-orbital model. Here we show the TB hamiltonian for high-energy  $dp$  models [3]. The basis here is  $(Ad_z, Bd_z, Ad_x, Bd_x, Ap_x, Bp_x, Ap_y, Bp_y, p_z, p_{z'}, p_{z''})$ . The position of these orbitals can be seen in Fig. A4. Here we show the elements of Hamiltonian  $H(\alpha, \beta)$

$$\begin{aligned}
 H(1, 9) &= t^{Ad_z, p_z}, H(2, 9) = t^{Bd_z, p_z}, H(1, 10) = t^{Ad_z, p_{z'}}, H(2, 11) = t^{Bd_z, p_{z''}}, \quad (3) \\
 H(3, 5) &= -2it^{Ad_x, Ap_x} \sin(0.5k_x), \quad H(3, 7) = -2it^{Ad_x - Ap_y} \sin(0.5k_y), \\
 H(4, 6) &= -2it^{Bd_x, Bp_x} \sin(0.5k_x), \quad H(4, 8) = -2it^{Bd_x - Bp_y} \sin(0.5k_y), \\
 H(1, 5) &= -2it^{Ad_z, Ap_x} \sin(0.5k_x), \quad H(1, 7) = -2it^{Ad_z - Ap_y} \sin(0.5k_y), \\
 H(2, 6) &= -2it^{Bd_z, Bp_x} \sin(0.5k_x), \quad H(2, 8) = -2it^{Bd_z - Bp_y} \sin(0.5k_y), \\
 H(5, 7) &= 4t^{Ap_x - Ap_y} \sin(0.5k_x) \sin(0.5k_y), \\
 H(6, 8) &= 4t^{Bp_x - Bp_y} \sin(0.5k_x) \sin(0.5k_y), \\
 H(5, 9) &= -2it^{Ap_x, p_z} \sin(0.5k_x), \quad H(7, 9) = -2it^{Ap_y, p_z} \sin(0.5k_y), \\
 H(6, 9) &= -2it^{Bp_x, p_z} \sin(0.5k_x), \quad H(8, 9) = -2it^{Bp_y, p_z} \sin(0.5k_y), \\
 H(5, 10) &= -2it^{Ap_x, p_{z'}} \sin(0.5k_x), \quad H(7, 10) = -2it^{Ap_y, p_{z'}} \sin(0.5k_y), \\
 H(6, 11) &= -2it^{Bp_x, p_{z''}} \sin(0.5k_x), \quad H(8, 11) = -2it^{Bp_y, p_{z''}} \sin(0.5k_y).
 \end{aligned}$$

The elements  $H(\beta, \alpha)$  can be obtained by  $H(\beta, \alpha) = H(\alpha, \beta)^*$ . The diagonal elements are site energies which can be found in Table 4 and Table 5.

### 3.3 Calculation of spin susceptibility

Upon determining the hopping parameters of the TB models and incorporating electron interactions, we construct a multi-orbital Hubbard model as Equation 1 without considering hoppings between two stacks.

$$\begin{aligned}\mathcal{H}_U = & U \sum_{is} n_{is\uparrow} n_{is\downarrow} \\ & + (U' - J_H \delta_{\sigma\sigma'}) \sum_{i\sigma\sigma'} (n_{iAx\sigma} n_{iAz\sigma'} + n_{iBx\sigma} n_{iBz\sigma'}) \\ & + J_H \sum_{i\sigma} \sum_{\mu}^{A,B} (d_{i\mu x\sigma}^\dagger d_{i\mu z\bar{\sigma}}^\dagger d_{i\mu x\bar{\sigma}} d_{i\mu z\sigma} \\ & + d_{i\mu x\sigma}^\dagger d_{i\mu x\bar{\sigma}}^\dagger d_{i\mu z\bar{\sigma}} d_{i\mu z\sigma} + h.c.).\end{aligned}\tag{4}$$

The TB Hamiltonian  $\mathcal{H}_0$  is expressed with the basis  $\Psi_\sigma = (d_{Ax\sigma}, d_{Az\sigma}, d_{Bx\sigma}, d_{Bz\sigma})$ , where  $d_{s\sigma}$  is the annihilation operator for an electron in the state  $s = (Ax, Az, Bx, Bz)$  with spin  $\sigma$ . The interaction parameters include  $U$  (intraorbital Coulomb interaction),  $U'$  (interorbital Coulomb interaction) and  $J_H$  (Hund's coupling). Kanamori relation is applied here, given by  $U' = U - 2J_H$  [66].

In general, the bare (non-interaction) susceptibility is defined as

$$\begin{aligned}\chi_{\alpha\beta\gamma\delta}^0(\mathbf{q}, \omega) = & -\frac{1}{N_{\mathbf{k}}} \sum_{\mathbf{k}, mn} \frac{f_F(\varepsilon_{\mathbf{k}}^m) - f_F(\varepsilon_{\mathbf{k}+\mathbf{q}}^n)}{i\omega + \varepsilon_{\mathbf{k}}^m - \varepsilon_{\mathbf{k}+\mathbf{q}}^n} \\ & U_{\delta m}(\mathbf{k}) U_{\alpha m}^*(\mathbf{k}) U_{\beta n}(\mathbf{k} + \mathbf{q}) U_{\gamma n}^*(\mathbf{k} + \mathbf{q}).\end{aligned}\tag{5}$$

with the band indices  $m, n$  and the Fermi-Dirac distribution function  $f_F(\varepsilon_{\mathbf{k}}) = 1/(e^{\varepsilon_{\mathbf{k}}/T} + 1)$ . The matrix element  $U_{\delta m}(\mathbf{k})$  represents the eigenvector connecting orbital  $\delta$  and band  $m$  at wave vector  $\mathbf{k}$ . At the RPA level, the spin channel interaction vertex is defined as

$$\Gamma_{\alpha\beta\gamma\delta}^m = \begin{cases} U & \alpha = \beta = \gamma = \delta, \\ U' & \alpha = \delta \neq \beta = \gamma, \\ J_H & \alpha = \beta \neq \gamma = \delta, \\ J' & \alpha = \gamma \neq \beta = \delta. \end{cases}\tag{6}$$

Here pair hopping  $J'$  satisfies  $J' = J_H$ . The RPA spin susceptibility is then computed in a matrix-product form as

$$\chi_{(\alpha\beta, \delta\gamma)}^S = \left[ I - \chi^0 \Gamma_{(\alpha\beta, \delta\gamma)}^m \right]^{-1} \chi_{(\alpha\beta, \delta\gamma)}^0.\tag{7}$$

Considering the bilayer structure of  $\text{La}_3\text{Ni}_2\text{O}_7$ , the interlayer hopping terms in the Hamiltonian acquire a phase factor of  $e^{ik_z}$  due to the  $k_z$ -dependence. Here,

$k_z$  can take values of either 0 or  $\pi$ . When contracting the orbital indices to compute the spin susceptibility, we define the in-plane and interlayer susceptibilities as  $\chi_{||} = \sum_{\alpha\beta}(\chi_{A\alpha A\beta} + \chi_{B\alpha B\beta})$  and  $\chi_{\perp} = \sum_{\alpha\beta}(\chi_{A\alpha B\beta} + \chi_{B\alpha A\beta})$ , where  $\chi_{\alpha\beta} = \chi_{\alpha\alpha\beta\beta}$  with orbital indices contracted. For  $k_z = 0$ , the phase factor  $e^{i0} = 1$ , and the spin susceptibility is given by  $\chi^e = \chi_{||} + \chi_{\perp}$ . Conversely, for  $k_z = \pi$ , the phase factor  $e^{i\pi} = -1$ , leading to a spin susceptibility of  $\chi^o = \chi_{||} - \chi_{\perp}$ . In the even channel  $\chi^e$ , Fermi surface nesting which occurs within the bonding/antibonding bands is evident, including the  $\alpha - \alpha$ ,  $\alpha - \gamma$ ,  $\gamma - \gamma$  and  $\beta - \beta$  nesting features. In the odd channel  $\chi^o$ , nesting between bonding and antibonding bands can be observed clearly, such as  $\gamma - \beta$ ,  $\alpha - \beta$  [57].

## 4 Discussion

Our DFT calculations of the thin-film bilayer nickelate superconductors have overall predicted the electronic structure closely resembles the bulk one under pressure, which strongly suggests that they all within the same superconducting mechanism. We note another key aspect to validate this idea, which is the superexchange strength. For the bulk samples, the vertical superexchange between two half-filling  $d_{z^2}$  orbitals  $J_{\perp}^z$  is widely believed to be the origin of the superconducting condensation [6, 7]. Here our TB models for the  $\text{La}_3\text{Ni}_2\text{O}_7$  thin-film also allow an estimation of the corresponding strengths, which are decreased by  $\sim 24\%$  and  $\sim 36\%$  for single-stacked and double-stacked bilayer nickelates with respect to the pressurized bulk [3], assuming  $J_{\perp}^z \sim (t^z)^2$ . The asymptotic decrease of  $J_{\perp}^z$  with slab number from our estimation is in line with the notable decrease of  $T_c$  from bulk to film as observed in experiments [47, 48], which again reinforce the above general understanding. More profoundly, the consistency indicates an expansion of the available experimental techniques for reaching the core of superconducting mechanism in RP nickelates. This is particularly helpful as the exploration on bulk is largely constrained by the exerted pressure. Regarding the role of pressure, on the other hand, the existing evidences on thin-film is also prone to the idea that pressure can help suppressing spin density wave, after which superconducting order is thus to expose. Whereas for the thin-film, due to the higher stability and stiffness of the  $\text{SrLaAlO}_4$  substrates,  $\text{La}_3\text{Ni}_2\text{O}_7$  lattice is strongly confined to the  $I4/mmm$  symmetry without inplane distortion, which can further prevent the occurrence of density waves [47, 48].

## 5 Conclusion

In conclusion, we employ slab models for  $\text{La}_3\text{Ni}_2\text{O}_7$  thin films that simulate the electronic structure for various thicknesses, including Three-UC, One-UC, and Half-UC. Each slab model incorporates a full unit cell, with the two bilayers referred to as Stack 1 and Stack 2, enabling a detailed examination of the interplay between dimensionality and electronic behaviors. Using density functional theory, we propose a double-stacked two-orbital effective model of  $\text{La}_3\text{Ni}_2\text{O}_7$  thin films, based on the  $\text{Ni}-e_g$  orbitals. Our analysis reveals the presence of three electron pockets  $\alpha, \alpha', \beta$  and two hole pockets  $\gamma, \gamma'$  on the Fermi surface, where the additional pockets  $\alpha'$  and  $\gamma'$  emerge due to inter-stack interactions. Furthermore, we introduce high-energy models incorporating  $\text{O}-p$

orbitals to facilitate future studies. Spin susceptibility calculations within the RPA indicate pronounced magnetic correlations primarily driven by nesting effects of the  $\gamma$  pocket, which is predominantly contributed by the Ni- $d_{z^2}$  orbital state. Our results provide theoretical framework for understanding the interplay among dimensionality, magnetism, and superconductivity in  $\text{La}_3\text{Ni}_2\text{O}_7$  thin films, offering key insights for future theoretical and experimental research.

## References

- [1] Sun, H., Huo, M., Hu, X., Li, J., Liu, Z., Han, Y., Tang, L., Mao, Z., Yang, P., Wang, B., *et al.*: Signatures of superconductivity near 80 K in a nickelate under high pressure. *Nature* **621**(7979), 493–498 (2023) <https://doi.org/10.1038/s41586-023-06408-7>
- [2] Zhu, Y., Peng, D., Zhang, E., Pan, B., Chen, X., Chen, L., Ren, H., Liu, F., Hao, Y., Li, N., Xing, Z., Lan, F., Han, J., Wang, J., Jia, D., Wo, H., Gu, Y., Gu, Y., Ji, L., Wang, W., Gou, H., Shen, Y., Ying, T., Chen, X., Yang, W., Cao, H., Zheng, C., Zeng, Q., Guo, J.-g., Zhao, J.: Superconductivity in pressurized trilayer  $\text{La}_4\text{Ni}_3\text{O}_{10-\delta}$  single crystals. *Nature* **631**(8021), 531–536 (2024) <https://doi.org/10.1038/s41586-024-07553-3>
- [3] Luo, Z., Hu, X., Wang, M., Wú, W., Yao, D.-X.: Bilayer two-orbital model of  $\text{La}_3\text{Ni}_2\text{O}_7$  under pressure. *Phys. Rev. Lett.* **131**(12), 126001 (2023) <https://doi.org/10.1103/PhysRevLett.131.126001>
- [4] Zhang, Y., Lin, L.-F., Moreo, A., Dagotto, E.: Electronic structure, dimer physics, orbital-selective behavior, and magnetic tendencies in the bilayer nickelate superconductor  $\text{La}_3\text{Ni}_2\text{O}_7$  under pressure. *Phys. Rev. B* **108**(18), 180510 (2023) <https://doi.org/10.1103/PhysRevB.108.L180510>
- [5] Lechermann, F., Gondolf, J., Bötzel, S., Eremin, I.M.: Electronic correlations and superconducting instability in  $\text{La}_3\text{Ni}_2\text{O}_7$  under high pressure. *Phys. Rev. B* **108**(20), 201121 (2023) <https://doi.org/10.1103/PhysRevB.108.L201121>
- [6] Luo, Z., Lv, B., Wang, M., Wú, W., Yao, D.-X.: High- $T_c$  superconductivity in  $\text{La}_3\text{Ni}_2\text{O}_7$  based on the bilayer two-orbital t-J model. *npj Quantum Mater.* **9**(1), 1–7 (2024) <https://doi.org/10.1038/s41535-024-00668-w>
- [7] Wú, W., Luo, Z., Yao, D.-X., Wang, M.: Superexchange and charge transfer in the nickelate superconductor  $\text{La}_3\text{Ni}_2\text{O}_7$  under pressure. *Sci. China Phys. Mech. Astron.* **67**(11), 117402 (2024) <https://doi.org/10.1007/s11433-023-2300-4>
- [8] Wang, M., Wen, H.-H., Wu, T., Yao, D.-X., Xiang, T.: Normal and superconducting properties of  $\text{La}_3\text{Ni}_2\text{O}_7$ . *Chin. Phys. Lett.* **41**(7) (2024) <https://doi.org/10.1088/0256-307X/41/7/077402>
- [9] Shilenko, D.A., Leonov, I.V.: Correlated electronic structure, orbital-selective

- behavior, and magnetic correlations in double-layer  $\text{La}_3\text{Ni}_2\text{O}_7$  under pressure. Phys. Rev. B **108**(12), 125105 (2023) <https://doi.org/10.1103/PhysRevB.108.125105>
- [10] Yang, Y.-f., Zhang, G.-M., Zhang, F.-C.: Interlayer valence bonds and two-component theory for high- $T_c$  superconductivity of  $\text{La}_3\text{Ni}_2\text{O}_7$  under pressure. Phys. Rev. B **108**(20), 201108 (2023) <https://doi.org/10.1103/PhysRevB.108.L201108>
  - [11] Huang, J., Wang, Z.D., Zhou, T.: Impurity and vortex states in the bilayer high-temperature superconductor  $\text{La}_3\text{Ni}_2\text{O}_7$ . Phys. Rev. B **108**(17), 174501 (2023) <https://doi.org/10.1103/PhysRevB.108.174501>
  - [12] Christiansson, V., Petocchi, F., Werner, P.: Correlated electronic structure of  $\text{La}_3\text{Ni}_2\text{O}_7$  under pressure. Phys. Rev. Lett. **131**(20), 206501 (2023) <https://doi.org/10.1103/PhysRevLett.131.206501>
  - [13] Shen, Y., Qin, M., Zhang, G.-M.: Effective bi-layer model hamiltonian and density-matrix renormalization group study for the high- $t_c$  superconductivity in  $\text{La}_3\text{Ni}_2\text{O}_7$  under high pressure. Chin. Phys. Lett. **40**(12), 127401 (2023) <https://doi.org/10.1088/0256-307X/40/12/127401>
  - [14] Oh, H., Zhang, Y.-H.: Type-II  $t - J$  model and shared superexchange coupling from hund's rule in superconducting  $\text{La}_3\text{Ni}_2\text{O}_7$ . Phys. Rev. B **108**(17), 174511 (2023) <https://doi.org/10.1103/PhysRevB.108.174511>
  - [15] Liu, Y.-B., Mei, J.-W., Ye, F., Chen, W.-Q., Yang, F.:  $s^\pm$ -wave pairing and the destructive role of apical-oxygen deficiencies in  $\text{La}_3\text{Ni}_2\text{O}_7$  under pressure. Phys. Rev. Lett. **131**(23), 236002 (2023) <https://doi.org/10.1103/PhysRevLett.131.236002>
  - [16] Liao, Z., Chen, L., Duan, G., Wang, Y., Liu, C., Yu, R., Si, Q.: Electron correlations and superconductivity in  $\text{La}_3\text{Ni}_2\text{O}_7$  under pressure tuning. Phys. Rev. B **108**(21), 214522 (2023) <https://doi.org/10.1103/PhysRevB.108.214522>
  - [17] Yang, Q.-G., Wang, D., Wang, Q.-H.: Possible  $s_\pm$ -wave superconductivity in  $\text{La}_3\text{Ni}_2\text{O}_7$ . Phys. Rev. B **108**(14), 140505 (2023) <https://doi.org/10.1103/PhysRevB.108.L140505>
  - [18] Chen, C.-Q., Luo, Z., Wang, M., Wú, W., Yao, D.-X.: Trilayer multiorbital models of  $\text{La}_4\text{Ni}_3\text{O}_{10}$ . Phys. Rev. B **110**, 014503 (2024) <https://doi.org/10.1103/PhysRevB.110.014503>
  - [19] Xu, S., Chen, C.-Q., Huo, M., Hu, D., Wang, H., Wu, Q., Li, R., Wu, D., Wang, M., Yao, D.-X., Dong, T., Wang, N.: Origin of the density wave instability in trilayer nickelate  $\text{La}_4\text{Ni}_3\text{O}_{10}$  revealed by optical and ultrafast spectroscopy. Phys. Rev. B **111**, 075140 (2025) <https://doi.org/10.1103/PhysRevB.111.075140>

- [20] Yang, J.-J., Yao, D.-X., Wu, H.-Q.: Correlation effects in a simplified bilayer two-orbital hubbard model at half filling. Phys. Rev. B **110**, 235155 (2024) <https://doi.org/10.1103/PhysRevB.110.235155>
- [21] Kaneko, T., Sakakibara, H., Ochi, M., Kuroki, K.: Pair correlations in the two-orbital hubbard ladder: Implications for superconductivity in the bilayer nickelate  $\text{La}_3\text{Ni}_2\text{O}_7$ . Phys. Rev. B **109**(4), 045154 (2024) <https://doi.org/10.1103/PhysRevB.109.045154>
- [22] Ouyang, Z., Gao, M., Lu, Z.-Y.: Absence of electron-phonon coupling superconductivity in the bilayer phase of  $\text{La}_3\text{Ni}_2\text{O}_7$  under pressure. npj Quantum Mater. **9**(1), 1–6 (2024) <https://doi.org/10.1038/s41535-024-00689-5>
- [23] Sakakibara, H., Ochi, M., Nagata, H., Ueki, Y., Sakurai, H., Matsumoto, R., Terashima, K., Hirose, K., Ohta, H., Kato, M., Takano, Y., Kuroki, K.: Theoretical analysis on the possibility of superconductivity in the trilayer ruddlesdenpopper nickelate  $\text{La}_4\text{Ni}_3\text{O}_{10}$  under pressure and its experimental examination: Comparison with  $\text{La}_3\text{Ni}_2\text{O}_7$ . Phys. Rev. B **109**, 144511 (2024) <https://doi.org/10.1103/PhysRevB.109.144511>
- [24] Heier, G., Park, K., Savrasov, S.Y.: Competing  $d_{xy}$  and  $s_{\pm}$  pairing symmetries in superconducting  $\text{La}_3\text{Ni}_2\text{O}_7$ : LDA + FLEX calculations. Phys. Rev. B **109**(10), 104508 (2024) <https://doi.org/10.1103/PhysRevB.109.104508>
- [25] Zhang, Y., Lin, L.-F., Moreo, A., Maier, T.A., Dagotto, E.: Structural phase transition,  $s_{\pm}$ -wave pairing, and magnetic stripe order in bilayered superconductor  $\text{La}_3\text{Ni}_2\text{O}_7$  under pressure. Nat Commun **15**(1), 2470 (2024) <https://doi.org/10.1038/s41467-024-46622-z>
- [26] Zhang, Y., Lin, L.-F., Moreo, A., Maier, T.A., Dagotto, E.: Electronic structure, magnetic correlations, and superconducting pairing in the reduced ruddlesdenpopper bilayer  $\text{La}_3\text{Ni}_2\text{O}_6$  under pressure: Different role of  $d_{3z^2-r^2}$  orbital compared with  $\text{La}_3\text{Ni}_2\text{O}_7$ . Phys. Rev. B **109**(4), 045151 (2024) <https://doi.org/10.1103/PhysRevB.109.045151>
- [27] Tian, Y.-H., Chen, Y., Wang, J.-M., He, R.-Q., Lu, Z.-Y.: Correlation effects and concomitant two-orbital  $s_{\pm}$ -wave superconductivity in  $\text{La}_3\text{Ni}_2\text{O}_7$  under high pressure. Phys. Rev. B **109**(16), 165154 (2024) <https://doi.org/10.1103/PhysRevB.109.165154>
- [28] Ryee, S., Witt, N., Wehling, T.O.: Quenched pair breaking by interlayer correlations as a key to superconductivity in  $\text{La}_3\text{Ni}_2\text{O}_7$ . Phys. Rev. Lett. **133**(9), 096002 (2024) <https://doi.org/10.1103/PhysRevLett.133.096002>
- [29] Zhang, J.-X., Zhang, H.-K., You, Y.-Z., Weng, Z.-Y.: Strong pairing originated from an emergent  $Z_2$  berry phase in  $\text{La}_3\text{Ni}_2\text{O}_7$ . Phys. Rev. Lett. **133**(12), 126501 (2024) <https://doi.org/10.1103/PhysRevLett.133.126501>



- [30] Ni, X.-S., Ji, Y., He, L., Xie, T., Yao, D.-X., Wang, M., Cao, K.: Spin density wave in the bilayered nickelate  $\text{La}_3\text{Ni}_2\text{O}_{7-\delta}$  at ambient pressure. *npj Quantum Materials* **10**(1), 1–9 (2025) <https://doi.org/10.1038/s41535-025-00740-z>
- [31] Lu, C., Pan, Z., Yang, F., Wu, C.: Interlayer-coupling-driven high-temperature superconductivity in  $\text{La}_3\text{Ni}_2\text{O}_7$  under pressure. *Phys. Rev. Lett.* **132**(14), 146002 (2024) <https://doi.org/10.1103/PhysRevLett.132.146002>
- [32] Qu, X.-Z., Qu, D.-W., Chen, J., Wu, C., Yang, F., Li, W., Su, G.: Bilayer  $t-J-J_\perp$  model and magnetically mediated pairing in the pressurized nickelate  $\text{La}_3\text{Ni}_2\text{O}_7$ . *Phys. Rev. Lett.* **132**(3), 036502 (2024) <https://doi.org/10.1103/PhysRevLett.132.036502>
- [33] Yang, H., Oh, H., Zhang, Y.-H.: Strong pairing from a small fermi surface beyond weak coupling: Application to  $\text{La}_3\text{Ni}_2\text{O}_7$ . *Phys. Rev. B* **110**(10), 104517 (2024) <https://doi.org/10.1103/PhysRevB.110.104517>
- [34] Fan, Z., Zhang, J.-F., Zhan, B., Lv, D., Jiang, X.-Y., Normand, B., Xiang, T.: Superconductivity in nickelate and cuprate superconductors with strong bilayer coupling. *Phys. Rev. B* **110**(2), 024514 (2024) <https://doi.org/10.1103/PhysRevB.110.024514>
- [35] Sakakibara, H., Kitamine, N., Ochi, M., Kuroki, K.: Possible high  $T_c$  superconductivity in  $\text{La}_3\text{Ni}_2\text{O}_7$  under high pressure through manifestation of a nearly half-filled bilayer hubbard model. *Phys. Rev. Lett.* **132**(10), 106002 (2024) <https://doi.org/10.1103/PhysRevLett.132.106002>
- [36] Cao, Y., Yang, Y.-f.: Flat bands promoted by hund’s rule coupling in the candidate double-layer high-temperature superconductor  $\text{La}_3\text{Ni}_2\text{O}_7$  under high pressure. *Phys. Rev. B* **109**(8), 081105 (2024) <https://doi.org/10.1103/PhysRevB.109.L081105>
- [37] Jiang, R., Hou, J., Fan, Z., Lang, Z.-J., Ku, W.: Pressure driven fractionalization of ionic spins results in cupratelike high- $T_c$  superconductivity in  $\text{La}_3\text{Ni}_2\text{O}_7$ . *Phys. Rev. Lett.* **132**(12), 126503 (2024) <https://doi.org/10.1103/PhysRevLett.132.126503>
- [38] Chen, X., Jiang, P., Li, J., Zhong, Z., Lu, Y.: Charge and spin instabilities in superconducting  $\text{La}_3\text{Ni}_2\text{O}_7$ . *Phys. Rev. B* **111**(1), 014515 (2025) <https://doi.org/10.1103/PhysRevB.111.014515>
- [39] Yang, J., Sun, H., Hu, X., Xie, Y., Miao, T., Luo, H., Chen, H., Liang, B., Zhu, W., Qu, G., Chen, C.-Q., Huo, M., Huang, Y., Zhang, S., Zhang, F., Yang, F., Wang, Z., Peng, Q., Mao, H., Liu, G., Xu, Z., Qian, T., Yao, D.-X., Wang, M., Zhao, L., Zhou, X.J.: Orbital-dependent electron correlation in double-layer nickelate  $\text{La}_3\text{Ni}_2\text{O}_7$ . *Nat Commun* **15**(1), 4373 (2024) <https://doi.org/10.1038/s41467-024-48701-7>

- [40] Zhang, Y., Su, D., Huang, Y., Shan, Z., Sun, H., Huo, M., Ye, K., Zhang, J., Yang, Z., Xu, Y., Su, Y., Li, R., Smidman, M., Wang, M., Jiao, L., Yuan, H.: High-temperature superconductivity with zero resistance and strange-metal behaviour in  $\text{La}_3\text{Ni}_2\text{O}_{7-\delta}$ . *Nat. Phys.* **20**, 1269–1273 (2024) <https://doi.org/10.1038/s41567-024-02515-y>
- [41] Hou, J., Yang, P.-T., Liu, Z.-Y., Li, J.-Y., Shan, P.-F., Ma, L., Wang, G., Wang, N.-N., Guo, H.-Z., Sun, J.-P., Uwatoko, Y., Wang, M., Zhang, G.-M., Wang, B.-S., Cheng, J.-G.: Emergence of high-temperature superconducting phase in pressurized  $\text{La}_3\text{Ni}_2\text{O}_7$  crystals. *Chin. Phys. Lett.* **40**(11), 117302 (2023) <https://doi.org/10.1088/0256-307X/40/11/117302>
- [42] Fan, S., Luo, Z., Huo, M., Wang, Z., Li, H., Yang, H., Wang, M., Yao, D.-X., Wen, H.-H.: Tunneling spectra with gaplike features observed in nickelate  $\text{La}_3\text{Ni}_2\text{O}_7$  at ambient pressure. *Phys. Rev. B* **110**, 134520 (2024) <https://doi.org/10.1103/PhysRevB.110.134520>
- [43] Wang, G., Wang, N.N., Shen, X.L., Hou, J., Ma, L., Shi, L.F., Ren, Z.A., Gu, Y.D., Ma, H.M., Yang, P.T., Liu, Z.Y., Guo, H.Z., Sun, J.P., Zhang, G.M., Calder, S., Yan, J.-Q., Wang, B.S., Uwatoko, Y., Cheng, J.-G.: Pressure-Induced Superconductivity In Polycrystalline  $\text{La}_3\text{Ni}_2\text{O}_{7-\delta}$ . *Phys. Rev. X* **14**(1), 011040 (2024) <https://doi.org/10.1103/PhysRevX.14.011040>
- [44] Liu, Z., Huo, M., Li, J., Li, Q., Liu, Y., Dai, Y., Zhou, X., Hao, J., Lu, Y., Wang, M., Wen, H.-H.: Electronic correlations and partial gap in the bilayer nickelate  $\text{La}_3\text{Ni}_2\text{O}_7$ . *Nat Commun* **15**(1), 7570 (2024) <https://doi.org/10.1038/s41467-024-52001-5>
- [45] Li, Q., Zhang, Y.-J., Xiang, Z.-N., Zhang, Y., Zhu, X., Wen, H.-H.: Signature of Superconductivity in Pressurized  $\text{La}_4\text{Ni}_3\text{O}_{10}$ . *Chin. Phys. Lett.* **41**(1), 017401 (2024) <https://doi.org/10.1088/0256-307X/41/1/017401>
- [46] Li, J., Peng, D., Ma, P., Zhang, H., Xing, Z., Huang, X., Huang, C., Huo, M., Hu, D., Dong, Z., Chen, X., Xie, T., Dong, H., Sun, H., Zeng, Q., Mao, H.-k., Wang, M.: Identification of the superconductivity in bilayer nickelate  $\text{La}_3\text{Ni}_2\text{O}_7$  upon 100 GPa. *arXiv* (2025). <https://doi.org/10.48550/arXiv.2404.11369>
- [47] Ko, E.K., Yu, Y., Liu, Y., Bhatt, L., Li, J., Thampy, V., Kuo, C.-T., Wang, B.Y., Lee, Y., Lee, K., Lee, J.-S., Goodge, B.H., Muller, D.A., Hwang, H.Y.: Signatures of ambient pressure superconductivity in thin film  $\text{La}_3\text{Ni}_2\text{O}_7$ . *Nature* **638**(8052), 935–940 (2025) <https://doi.org/10.1038/s41586-024-08525-3>
- [48] Zhou, G., Lv, W., Wang, H., Nie, Z., Chen, Y., Li, Y., Huang, H., Chen, W., Sun, Y., Xue, Q.-K., Chen, Z.: Ambient-pressure superconductivity onset above 40 K in  $(\text{La,Pr})_3\text{Ni}_2\text{O}_7$  films. *Nature* (2025) <https://doi.org/10.1038/s41586-025-08755-z>
- [49] Liu, Z., Huo, M., Li, J., Li, Q., Liu, Y., Dai, Y., Zhou, X., Hao, J., Lu,

- Y., Wang, M., *et al.*: Electronic correlations and partial gap in the bilayer nickelate  $\text{La}_3\text{Ni}_2\text{O}_7$ . *Nat Commun* **15**(1), 7570 (2024) <https://doi.org/10.1038/s41467-024-52001-5>
- [50] Liu, Y., Ko, E.K., Tarn, Y., Bhatt, L., Goodge, B.H., Muller, D.A., Raghu, S., Yu, Y., Hwang, H.Y.: Superconductivity and normal-state transport in compressively strained  $\text{La}_2\text{PrNi}_2\text{O}_7$  thin films (2025). <https://arxiv.org/abs/2501.08022>
- [51] Bhatt, L., Jiang, A.Y., Ko, E.K., Schnitzer, N., Pan, G.A., Segedin, D.F., Liu, Y., Yu, Y., Zhao, Y.-F., Morales, E.A., Brooks, C.M., Botana, A.S., Hwang, H.Y., Mundy, J.A., Muller, D.A., Goodge, B.H.: Resolving Structural Origins for Superconductivity in Strain-Engineered  $\text{La}_3\text{Ni}_2\text{O}_7$  Thin Films (2025). <https://arxiv.org/abs/2501.08204>
- [52] Li, P., Zhou, G., Lv, W., Li, Y., Yue, C., Huang, H., Xu, L., Shen, J., Miao, Y., Song, W., Nie, Z., Chen, Y., Wang, H., Chen, W., Huang, Y., Chen, Z.-H., Qian, T., Lin, J., He, J., Sun, Y.-J., Chen, Z., Xue, Q.-K.: Photoemission evidence for multi-orbital hole-doping in superconducting  $\text{La}_{2.85}\text{Pr}_{0.15}\text{Ni}_2\text{O}_7/\text{SrLaAlO}_4$  interfaces (2025). <https://arxiv.org/abs/2501.09255>
- [53] Yue, C., Miao, J.-J., Huang, H., Hua, Y., Li, P., Li, Y., Zhou, G., Lv, W., Yang, Q., Sun, H., Sun, Y.-J., Lin, J., Xue, Q.-K., Chen, Z., Chen, W.-Q.: Correlated electronic structures and unconventional superconductivity in bilayer nickelate heterostructures (2025). <https://arxiv.org/abs/2501.06875>
- [54] Shao, Z.-Y., Liu, Y.-B., Liu, M., Yang, F.: Band Structure and Pairing Nature of  $\text{La}_3\text{Ni}_2\text{O}_7$  Thin Film at Ambient Pressure (2025). <https://arxiv.org/abs/2501.10409>
- [55] Georges, A., Medici, L.d., Mravlje, J.: Strong correlations from hunds coupling. *Annual Review of Condensed Matter Physics* **4**(1), 137–178 (2013) <https://doi.org/10.1146/annurev-conmatphys-020911-125045>
- [56] Löwdin, P.: A Note on the Quantum-Mechanical Perturbation Theory. *J. Chem. Phys.* **19**(11), 1396–1401 (2004) <https://doi.org/10.1063/1.1748067>
- [57] Bötzel, S., Lechermann, F., Gondolf, J., Eremin, I.M.: Theory of magnetic excitations in the multilayer nickelate superconductor  $\text{La}_3\text{Ni}_2\text{O}_7$ . *Phys. Rev. B* **109**, 180502 (2024) <https://doi.org/10.1103/PhysRevB.109.L180502>
- [58] Kresse, G., Hafner, J.: Ab initio molecular dynamics for liquid metals. *Phys. Rev. B* **47**, 558–561 (1993) <https://doi.org/10.1103/PhysRevB.47.558>
- [59] Kresse, G., Furthmüller, J.: Efficient iterative schemes for ab initio total-energy calculations using a plane-wave basis set. *Phys. Rev. B* **54**, 11169–11186 (1996) <https://doi.org/10.1103/PhysRevB.54.11169>

- [60] Perdew, J.P., Burke, K., Ernzerhof, M.: Generalized gradient approximation made simple. *Phys. Rev. Lett.* **77**, 3865–3868 (1996) <https://doi.org/10.1103/PhysRevLett.77.3865>
- [61] Böchl, P.E.: Projector augmented-wave method. *Phys. Rev. B* **50**, 17953–17979 (1994) <https://doi.org/10.1103/PhysRevB.50.17953>
- [62] Pizzi, G., Vitale, V., Arita, R., Blügel, S., Freimuth, F., Géranton, G., Gibertini, M., Gresch, D., Johnson, C., Koretsune, T., Ibañez-Azpiroz, J., *et al.*: Wannier90 as a community code: new features and applications. *J. Phys.: Condens. Matter* **32**(16), 165902 (2020) <https://doi.org/10.1088/1361-648x/ab51ff>
- [63] Marzari, N., Vanderbilt, D.: Maximally localized generalized wannier functions for composite energy bands. *Phys. Rev. B* **56**, 12847–12865 (1997) <https://doi.org/10.1103/PhysRevB.56.12847>
- [64] Souza, I., Marzari, N., Vanderbilt, D.: Maximally localized wannier functions for entangled energy bands. *Phys. Rev. B* **65**, 035109 (2001) <https://doi.org/10.1103/PhysRevB.65.035109>
- [65] Dudarev, S.L., Botton, G.A., Savrasov, S.Y., Humphreys, C.J., Sutton, A.P.: Electron-energy-loss spectra and the structural stability of nickel oxide: An LSDA+U study. *Phys. Rev. B* **57**, 1505–1509 (1998) <https://doi.org/10.1103/PhysRevB.57.1505>
- [66] Georges, A., Medici, L.d., Mravlje, J.: Strong correlations from hund’s coupling. *Annual Review of Condensed Matter Physics* **4**(Volume 4, 2013), 137–178 (2013) <https://doi.org/10.1146/annurev-conmatphys-020911-125045>

**Acknowledgements.** We are grateful to Wéi Wú and Xiao-Hong Pan for useful discussions. Work at Sun Yat-Sen University was supported by the National Natural Science Foundation of China (Grants No. 12494591, No. 92165204), the National Key Research and Development Program of China (Grant No. 2022YFA1402802), Guangdong Provincial Key Laboratory of Magnetoelectric Physics and Devices (Grant No. 2022B1212010008), Research Center for Magnetoelectric Physics of Guangdong Province (Grant No. 2024B0303390001), Guangdong Provincial Quantum Science Strategic Initiative (Grant No. GDZX2401010), and Leading Talent Program of Guangdong Special Projects (201626003).

**Author contributions.** D.X.Y. and X.H. proposed and designed the project. X.H. and C.Q.C. contributed to DFT calculations. X.H. and D.X.Y. contributed to two-orbital models. W.Q. and D.X.Y. contributed to high-energy models. W.Q. and Z.L. contributed to spin susceptibility and discussion under the supervision of D.X.Y. All authors contributed to the interpretation of the results and wrote the paper.

**Competing interests.** The authors declare no competing interests.

**Materials and Correspondence.** Correspondence and requests for materials should be addressed to D.X.Y.

## Appendix A Band structures

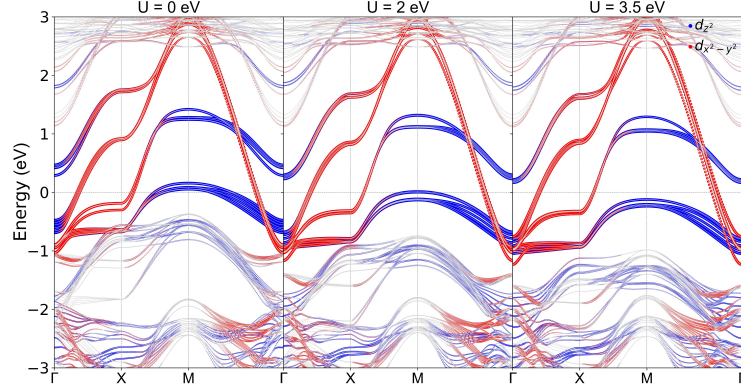


**Fig. A1** The DFT-calculated band structures for Three-UC, where panels (a), (b), and (c) are correspond to  $U = 0, 2$ , and  $3.5$  eV, respectively. The  $E_F$  is set to  $0$  eV.

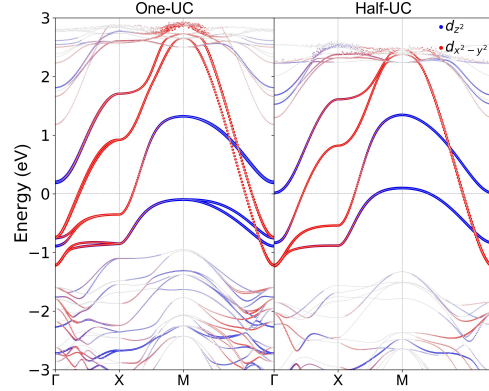


**Fig. A2** The DFT-calculated band structures for (a) One-UC and (b) Half-UC in the case of  $U = 3.5$  eV. The  $E_F$  is set to  $0$  eV.

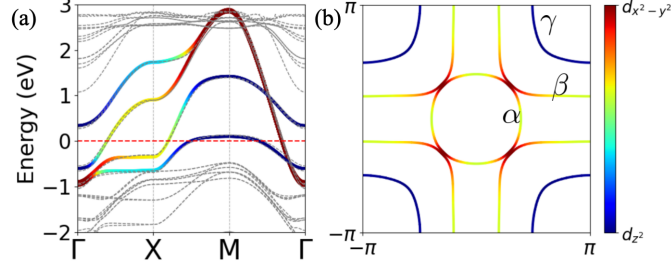


**Fig. A3** (a) Band structure along the high-symmetry path and (b) Fermi surface of the double-stacked two-orbital model in the absence of inter-stack hopping.

Here, we present the band structure and Fermi surface of the double-stacked two-orbital model without inter-stack hopping. As shown in Fig. A3 and Fig. 4, the inclusion of inter-stack hopping leads to the splitting of  $\gamma$  pocket into two distinct pockets, with the primary differences emerging along the  $M - \Gamma$  direction. Similarly, the  $\alpha$  pocket also undergoes splitting, however, the resulting pockets remain nearly identical.

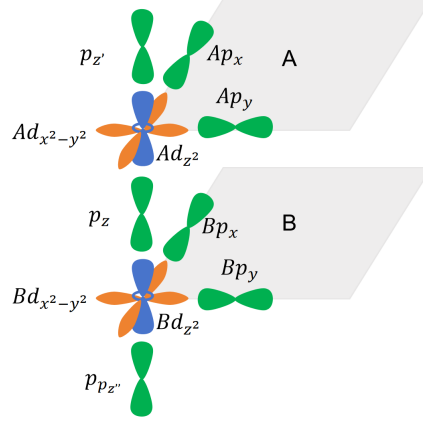


**Fig. A4** Schematic representation of Stack 1 for the eleven-orbital model and twenty-two-orbital models. Ni- $d_{z^2}$  and Ni- $d_{x^2-y^2}$  orbitals are depicted in blue and orange, respectively, while all oxygen orbitals are shown in green.